7.1 Introduction

The importance of Ag, Cu and their bimetallic nanoparticles in catalytic reactions has already been discussed in previous chapters. Synthesis of pure noble metal (monometallic or bimetallic) nanoparticles requires stabilizers to protect them against aggregation. Stabilizers are not required if the nanoparticles are synthesized on a support material by heterogeneous nucleation [Guerra and Herrero (2010)]. The immobilization of these nanoparticles on to the support materials is a favored approach for making them easily separable and thereby recyclable [Vats *et al.* (2017)]. On the other hand, the support material may not be inert with respect to the reactant/substrate molecule. In that case the support will also impart its own property to the resulting catalyst. This may improve or result in a decline in the catalytic property of the composite particles.

Variety of support materials such as metal−organic frameworks, carbon based materials, metal oxides and zeolites have been used to immobilize metal NPs to study their improved catalytic properties [Moteki *et al.* (2011), Corma *et al.* (2010), Zheng and Stucky (2006), Schubert *et al*. (2001)]. Many recent studies on carbon based materials like graphene derivatives, carbon nanotubes, porous carbons, carbon nanofibers, carbon spheres, etc. have revealed that these are good support materials for loading the catalyst. These support materials exhibit high surface area, well-defined porosity, and strong interaction of support material with NPs. In view of this, it is expected that these support materials would demonstrate good adsorption properties in general.

Among various carbon supports, graphene oxide (GO) offers oxygen containing functional groups (hydroxyl, carbonyl, and carboxylic groups), which can offer abundant sites for adsorbing metal ions and then their heterogeneous nucleation to metal NPs. The

reduction of GO gives reduced GO (rGO). This material is nearer to graphene that has very good electrical conductivity properties. In spite of these advantages, there is lack of studies on the syntheses of highly dispersed noble metal NPs with high catalytic activity on rGO-based support materials. There are reports on the synergistic effect of metal loaded on reduced graphene oxide [Chen *et al.* (2011)]. CuNPs and AgNPs loaded on rGO have shown excellent peroxidase-like properties [Tan *et al.* (2014), Jiang *et al.* (2012)]. Further, as discussed before (Chapter-6), bimetallic NPs also display the synergistic effect in catalysis in comparison to their monometallic equivalents. There is report on the loading of Cu-Ag bimetallic NPs onto rGO sheets with improved chemical and physical properties of bimetallic Cu-Ag/rGO composite due to the synergistic effects of all the three components in peroxidase mimic towards detection of glucose and ascorbic acid [Darabdhara *et al.* (2017)]. Composite of graphene derivatives with metal NPs acts as visible light photocatalyst in degradation of dyes [Maryami *et al.* (2016)]. Wang *et al.* (2014) reported Pd-based bimetallic nanocomposites with graphene for electrocatalytic oxygen reduction reaction. Feng *et al.* (2011) also reported the synthesis of Pt-Ag alloy-graphene hybrid composite and studied its catalytic activity in methanol electrooxidation.

The support effect on catalyzing the nitro aromatics reduction to their corresponding azo compounds is also reported [Maddinedi *et al*. (2017)]. Zirconium oxide (ZrO_2) supported AuNPs was employed as catalyst for nitro aromatics reduction to azo compounds under mild conditions through visible light irradiation [Zhu *et al.* (2010)]. Due to visible light absorption electron excitation takes place in NPs which activates the adsorbates on the NPs. There are also reports on AgNPs on support materials used as an efficient photocatalyst under ultraviolet and visible light irradiation [Chen *et al.* (2010b), Tada *et al.* (2005)]. Graphene

possess highly conducting surface which offers high mobility of photogenerated energetic charge carriers, therefore slows the recombination of photogenerated electron-hole pair. Thus, CuNPs supported on graphene were found to exhibit high photocatalytic activity for the reductive coupling of nitro aromatics to aromatic azo compounds under irradiation of solar spectrum [Guo *et al.* (2014)].

This chapter deals with the synthesis of Ag, Cu and Ag-Cu BNPs supported on reduced grapheme oxide through chemical reduction route. Further, catalytic properties of reduced grapheme oxide with monometallic and bimetallic Ag and Cu NPs is discussed for *p*-nitrophenol (Nip) reduction and methyl orange (MO) oxidation reactions Activation energies of these rGO-composite catalyzed reduction and oxidation reactions have also been found. The photocatalytic enhancement when these reactions are carried out under visible light is also discussed for the MO oxidation reaction.

7.2 Experimental

7.2.1 Synthesis of graphene oxide (GO)

For the synthesis of GO, a mixture of graphite flakes (3.0 g) and $KMnO_4$ (18.0 g) were added to a 9 : 1 mixture of concentrated H_2SO_4/H_3PO_4 (360 : 40 mL). This reaction was then subjected to heat treatment at 50 °C for 12 hours with continuous stirring. The reaction mixture was then cooled to room temperature and poured into ice. Further, 30 % H_2O_2 (3 mL) was added until there was a color change from red to orange. The reaction solution was centrifuged (4400 rpm for 15 min) and the supernatant was decanted away. The remaining solid material was then washed in successively by water (3x) and ethanol (1x). Following this, the product was dried in the vacuum oven for 12h and ground to a fine powder.

7.2.2 Synthesis of M (mono or bimetallic Ag/Cu)-rGO composites

Materials used for the synthesis of M/rGO composite NPs were $AgNO_3$ (Merck), $Cu(NO_3)_2.3H_2O$ (Merck), Polyvinylpyrrolidone (PVP) (Himedia), NaOH (Merck), Ammonia (Merck) and Hydrazine Hydrate (Merck). All reagents used were of analytical reagent grade and used without further purification. Firstly, equal volumes of 0.0125 M NaOH and 0.25 M hydrazine hydrate were mixed to prepare the alkaline hydrazine hydrate (AHH) solution. 60 mL of 0.01 M $Ag(NO_3)$ and 60 mL of GO (0.65mg/mL) were taken in a three necked flask and stirred for 15 hours at room temperature. 0.3 g PVP in 60 mL water was then added in the above reaction mixture. N_2 gas was purged for 30 minutes to provide an inert environment. This reaction mixture flask was kept in a preheated water bath maintained at 333 K. Then 16 mL of AHH solution was added in a drop wise manner to this reaction mixture with continuous stirring. Grey colored precipitate was formed. The stirring was continued for 10 min more under N_2 environment. This composite sample was denoted as G1. This reaction mixture was cooled and centrifuged at 10000 rpm followed by washing with ethanol. The same procedure was adopted to prepare Cu/rGO. Only, instead of $AgNO_3$, suitable Cu^{2+} salt was added. As the reaction progresses, the initially blue colored copper salt solution changes to orange and then to reddish brown. This Cu/rGO composite sample is hereafter denoted by G5.

To obtain Ag-Cu BNPs/rGO composite, first 60 mL 0.01 M $Cu(NO_3)_2$ and 60 ml GO was stirred at room temperature for 15 hours. Hereafter, 0.3 g in 60 mL water PVP solution was added to the above solution and N_2 gas was bubbled through the reaction mixture for 30 min. The $Ag(NH_3)_2^+$ complex (prepared by adding equal volumes of 0.01 M $Ag(NO_3)$ solution and 0.02 M NH_3 solution) solution was added to 60 mL GO and then stirred for 15

hours. This mixture and the AHH solution were then added to the Cu^{2+} salt-GO mixture (prepared earlier) kept in a preheated oil bath maintained at 333 K. Continuous N_2 purging was resorted to throughout the process. As the reaction progressed, the reaction first turned orange then to brown color. After completion of this addition, the resulting reaction mixture was stirred for 10 min more. Finally, the precipitate formed was separated out by centrifuging at 10000 rpm. The precipitate was washed repeatedly with ethanol and then vacuum dried at 323 K. Three Ag-Cu BNPs /rGO composite samples were prepared in this manner. The $Ag(NH_3)_2^+$ to $Cu(NO_3)_2$ salt solution ratio was 2 : 1, 1 : 1 and 1 : 2 in samples denoted by G2, G3 and G4 respectively.

7.2.3 Catalytic reduction and oxidation

7.2.3.1 Catalytic Nip reduction with $NaBH_4$

The experimental details for the Nip reduction with $NaBH_4$ in presence of the above prepared M/rGO composite particles is identical to the protocol described in sub-section 3.2.2.1 of Chapter-3. 50 μL of the as prepared M/rGO sol was added to the reaction mixture for its catalytic study.

7.2.3.2 Catalytic Nip reduction with glycerol

The particulars of experiments for the Nip reduction with Gly as reductant in presence of M/rGO composite particles as catalyst is identical to the protocol described in sub-section 3.2.2.2 of Chapter-3.

7.2.3.3 Catalytic oxidation of MO dye

The experimental details for the oxidative MO degradation with H_2O_2 in presence of M/rGO composite particles is identical to the protocol described in sub-section 3.2.2.3 of Chapter-3.

7.2.4 Visible light enhancement of catalytic reduction and oxidation activites

Photocatalytic activity was measured by placing the reaction mixture in a four sided quartz cuvette in the photocatalytic chamber such that the reaction mixture was exposed from all the four sides to cool white LED light as per the setup given in Chapter-2. The temperature of the photocatalytic chamber was 306 K.

7.2.4.1 Photocatalytic enhancement in Nip reduction with glycerol

The reaction mixture with the catalyst was prepared as given in section 3.2.2.2. The reaction mixture was then irradiated by visible light from cool white LED source (approximately 940 watts/m^2) in the photocatalytic chamber at 306 K.

7.2.4.2 Photocatalytic oxidation of methyl orange dye

The reaction mixture with the catalyst was prepared as given in section 3.2.2.3. The reaction mixture was kept in the photocatalytic chamber at 306 K and then irradiated by visible light from cool white LED source (approximately 940 watts/m^2).

7.3 Results and discussions

7.3.1 Characterization of grapheme oxide (GO)

The XRD graph of GO is shown in Figure 7.1. XRD shows the characteristic reflection of GO at 2θ = 9.55 [Bo *et al.* (2014)]. Further, the UV-visible absorbance spectra of GO and rGO are shown in Figure 7.2. It shows a peak at 228 nm corresponding to GO [Jana *et al.*

(2014)]. On the other hand, rGO shows a red shift in absorbance spectra (~ 270 nm) which is in agreement with the literature reports [Jana *et al.* (2014)].

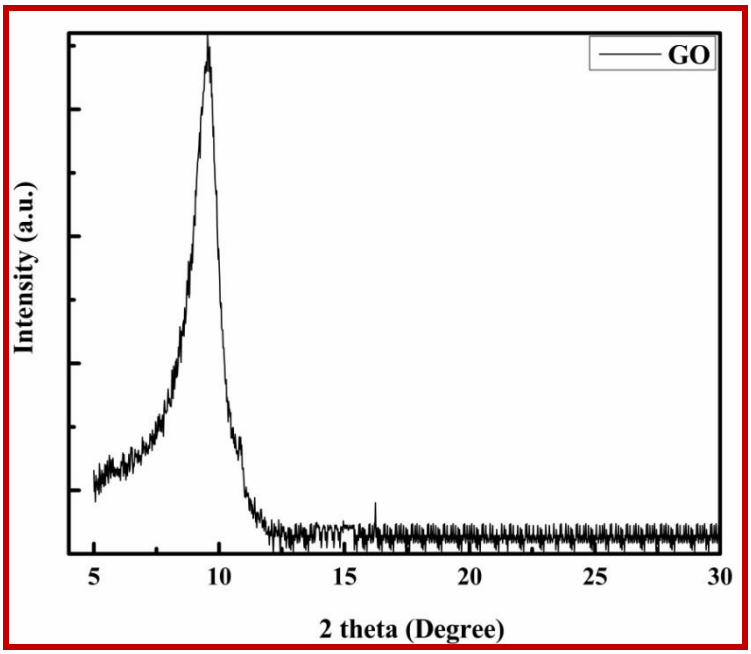

Figure 7.1 XRD of prepared GO sample.

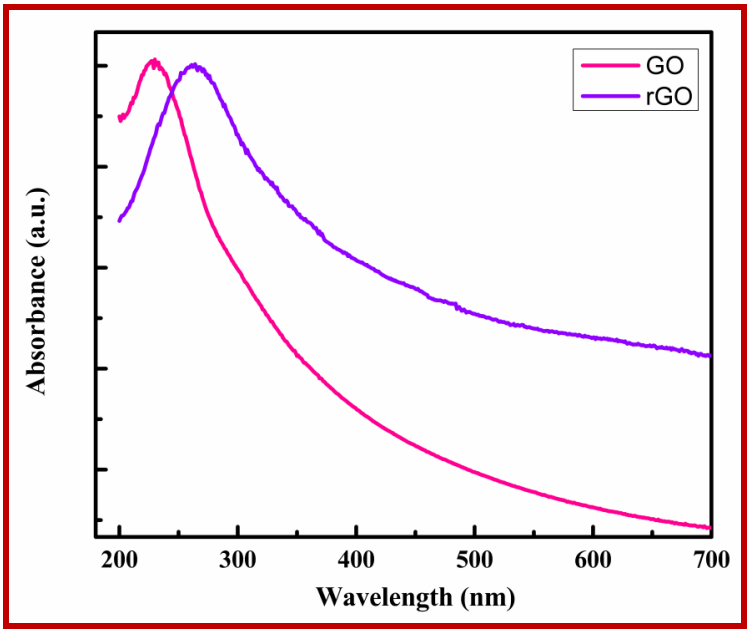

Figure 7.2 UV-visible absorption spectra of GO and rGO.

7.3.2 Characterization of M/rGO composite

X-ray diffraction patterns of the nanoparticle powder samples G1, G2, G3, G4 and G5 are shown in Figure 7.3 (a). G1 sample shows four peaks at 2θ = 38.18°, 44.40°, 64.66° and 77.07° corresponding to the {111}, {200}, {220} and {311} planes of FCC silver. Samples G2, G3 and G4 shows four peaks at 2θ = 38.18°, 44.40°, 64.66° and 77.07° corresponding to the {111}, {200}, {220} and {311} planes of FCC silver and one peak at 2θ = 43.23 corresponding to {111} planes of FCC copper. Further, in Sample G5 three peaks were observed at 2θ = 43.23°, 51.02° and 74.13° corresponding to {111}, {200} and {220} planes of FCC copper. The results for G2, G3 and G4 show that both Ag and Cu are present in these samples. Further, as discussed above the XRD peak at 2θ = 10.11° corresponding to GO in Figure 7.1 is disappeared completely. A broad peak at 2θ = 22-24° is present in all five samples (G1, G2, G3, G4 and G5) which is due to the formation of rGO.

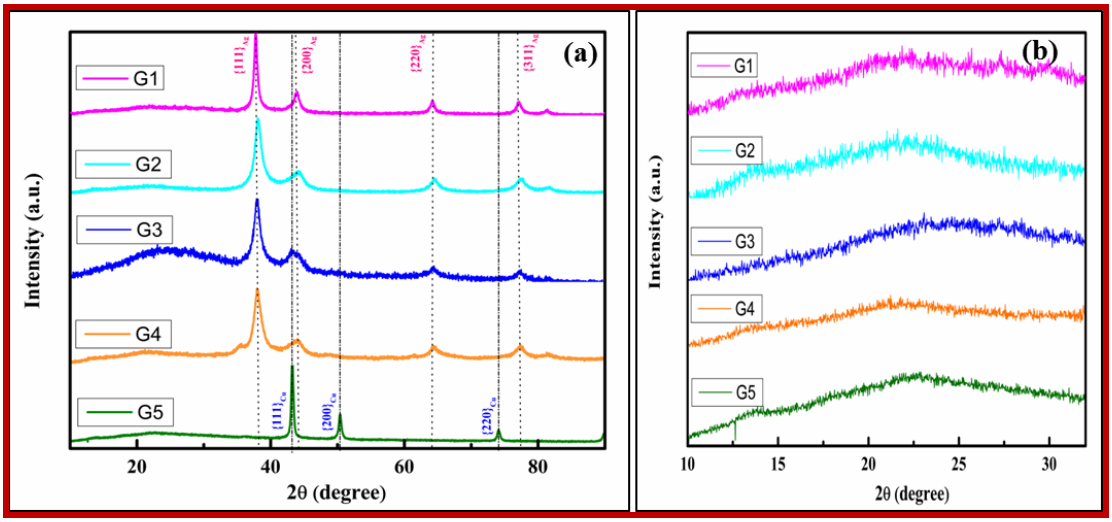

Figure 7.3 XRD pattern of G1, G2, G3 G4 and G5 powder samples (a) and diffuse rGO peak in all five samples (b).

The UV-visible spectra of G1, G2, G3, G4 and G5 sol samples are shown in Figure 7.4. Sample G1 shows peak absorbance at ~ 412 nm conforming to the LSPR exhibited by

AgNPs. Sample G2, G3 and G4 shows two LSPR peaks, one corresponding to AgNPs and other corresponding to CuNPs. In G2 a sharp peak corresponding to Ag is observed at 398 and a small peak corresponding to Cu is observed at ~ 577 nm. Both LSPR maximums are slightly blue shifted. Sols of G3 and G4 also show the presence of both Ag and Cu peaks. In G4 the LSPR corresponding to Ag is observed at ~ 386 nm. But the LSPR corresponding to Cu is same in both G3 and G4 at ~ 582 nm. It is important to note that the intensity of the peak corresponding to Cu (relative to LSPR maximum peak of Ag) in the LSPR's of G2, G3 and G4, increase with the proportion of Cu present in the sample. The absorbance maximum observed at ~ 271 nm is due to rGO.

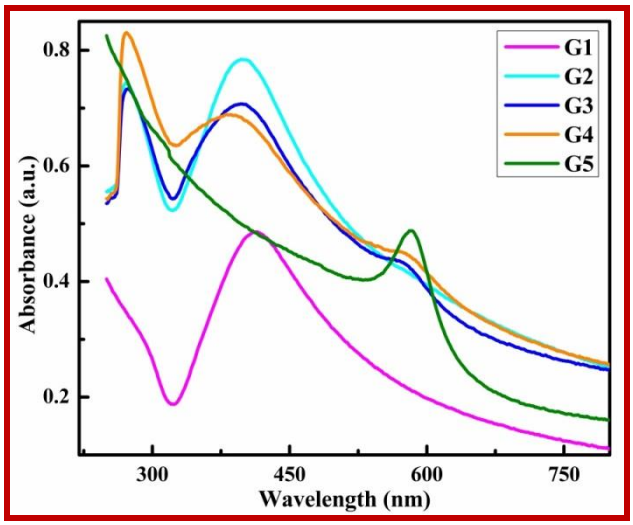

Figure 7.4 UV-visible absorbance spectra of aqueous dispersion of G1, G2, G3, G4 and G5 sol samples.

TEM micrographs of G1, G2, G3, G4 and G5 M-rGO composite samples are shown in Figure 7.5. All images shows the particles are attached to the rGO. Majority of these are almost spherical in shape. The average particle sizes for G1, G2, G3, G4 and G5 are ~25, ~ 30, ~ 40, ~ 35 and ~ 45 nm respectively.

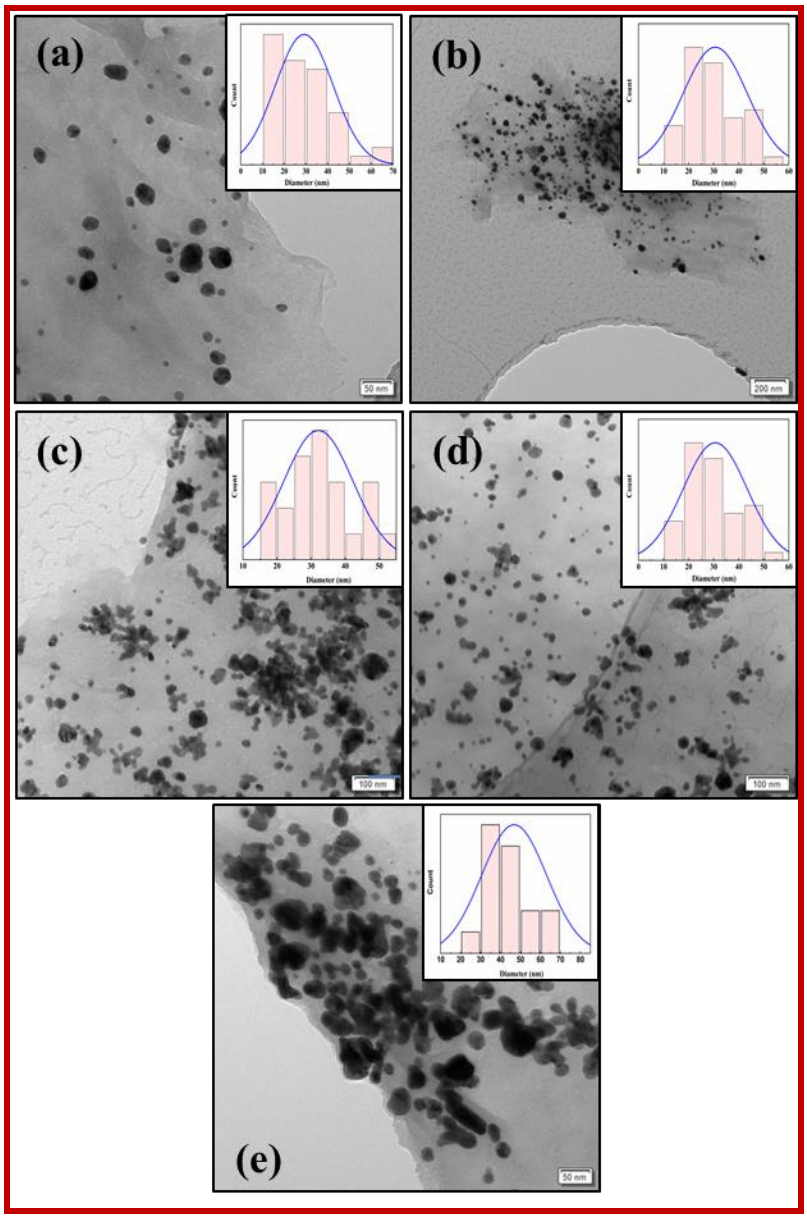

Figure 7.5 TEM images of G1, G2, G3, G4 and G5 samples are represented as **7 (a), 7 (b), 7 (c), 7 (d)** and **7 (e)** respectively, their corresponding size distribution histograms are shown in the inset of each micrograph.

The nanostructures formed G2, G3 and G4 samples are also of similar shape and sizes, therefore we did HR-SEM EDX elemental mapping (Figure 7.6) of these nanoparticles to confirm the presence of both Ag and Cu components. Figure 7.6 (a), 6 (c) and 6 (e) shows

the area for samples G2, G3 and G4 samples respectively. The inset of each SEM image shows the particular nanoparticle for which elemental mapping was done. The corresponding SEM EDX elemental mapping of the samples G2, G3 and G4 (Figure 7.6 (b), 6(d) and 6(f) respectively) show the presence of both Ag (depicted by red pixels) and Cu (represented by cyan pixels) in the mapped nanoparticle.

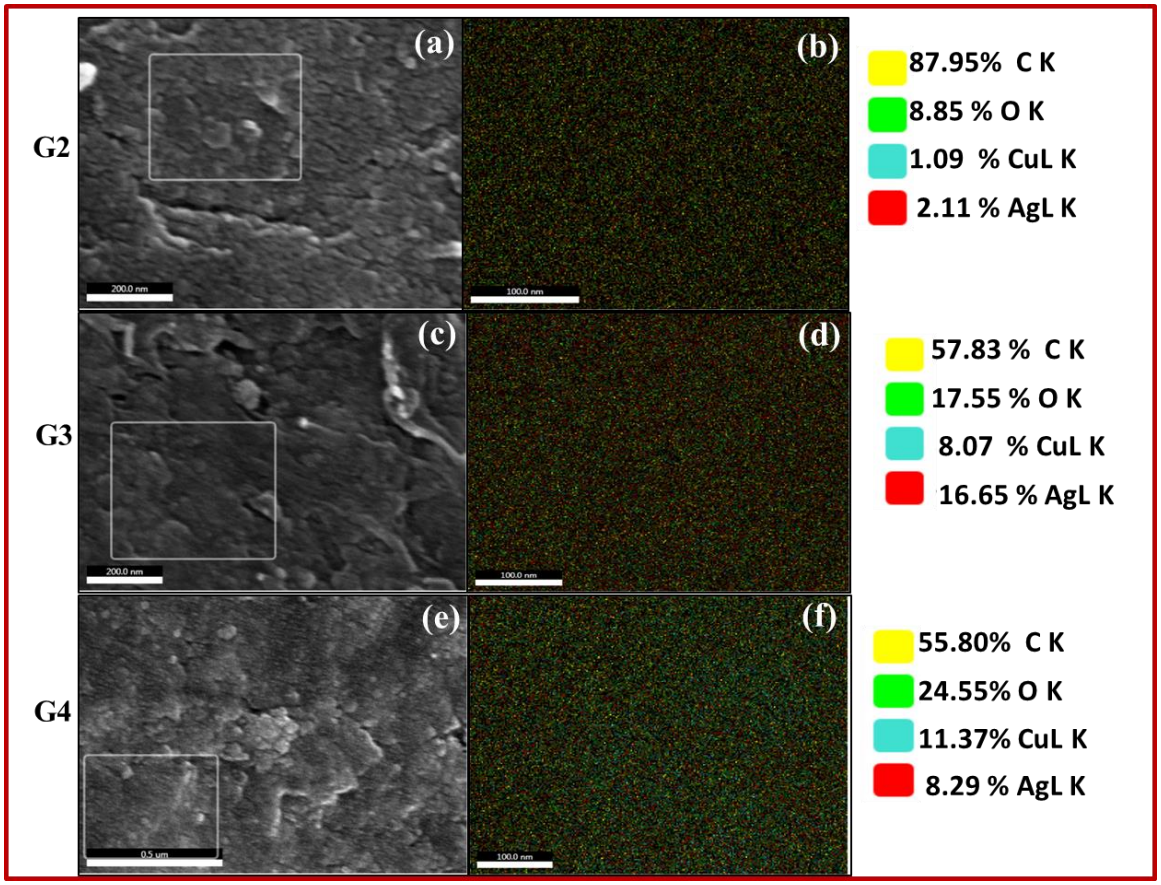

Figure 7.6 HR-SEM images shows the area on which mapping was done for G2, G3 and G4 samples **(6 (a), 6 (b), 6 (c))** and corresponding elemental mapping of particles **(6 (d), 6 (e) , 6 (f))** respectively.

7.3.3 Catalytic reduction and oxidation

7.3.3.1 Catalytic Activity of M/rGO composites for Nip reduction with $NaBH_4$ and Gly

The Nip reduction experiment is done with $NaBH_4$ as the reducing agent in presence of prepared catalyst. Here the intensity of absorbance at ~ 401 nm (*p*-nitrophenolate ion) was found to decrease with time. Simultaneously there was increase in the intensity of a new absorbance peak at ~ 301 nm due to formation of AP (Figure 7.7). In case of Nip reduction by glycerol the absorbance maximum at ~ 404 nm did not change with time till 150 min, this means that the reduction is not proceeding with these composites of rGO.

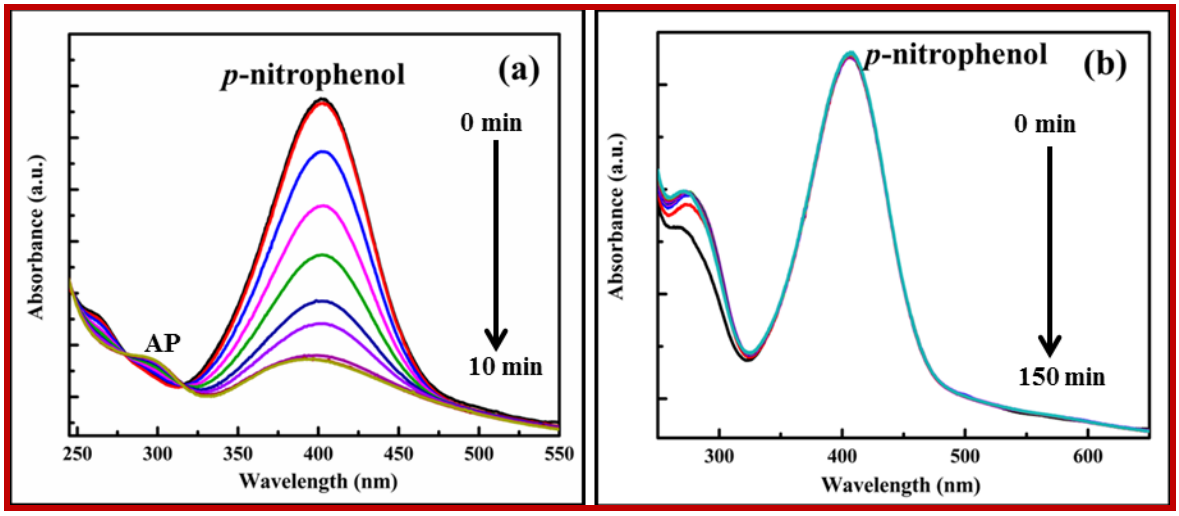

Figure 7.7 Variation of absorbance maximum of *p*-nitrophenolate (~ 401 nm) with $NaBH_4$ **7 (a)** and absorbance maximum of *p*-nitrophenolate (~ 406 nm) with Gly **7 (b)** as reductant in presence of G3 catalyst.

It may be recalled from Chapter-6, that Nip (thermal) reduction by Gly did not occur when BNPs were used as catalysts. However, in presence of BNPs/rGO composites no reduction of Nip by Gly takes place. A fundamental requirement for heterogeneous catalysis to occur is that the reactants should adsorb on the surface of the catalyst material. On comparing the results presented in this Chapter with that of Chapter-6 (for this reaction), it

may be concluded that the adsorption of Gly on rGO on is very poor. Therefore, this material is unable to catalyze the reaction between Nip and Gly.

The plot between $\ln(-\frac{\partial A}{\partial t})$ versus $\ln(A)$, the relation given in Chapter-3 [Eqn.3.3] gives the value of n. The value of n is found to be 1 when the reduction is carried out with $NaBH_4$ as reducing agent. Therefore, the kinetic plot between $\ln(A/A_0)$ and time are linear for G1, G2, G3, G4 and G5 catalyzed reaction (Figure 7.8 (a)). As already mentioned this reduction follows pseudo first-order kinetics in presence of majority of catalyst (monometallic or bimetallic), in agreement with the previous reports in literature [Deka *et al*. (2014), Yang *et al*. (2014)]. The kinetics plot for Nip reduction by $NaBH_4$ in presence of G1, G2, G3, G4 and G5 catalysts shows that there is no change in the initial absorbance of *p*-nitrophenolate for some interval of time. As mentioned earlier, the reason for such induction time could be oxygen adsorption on the surface of the metal or bimetallic catalysts. The slope of the linear fit (excluding induction time) obtained in Figure 7.8 (a) gives k_{app} values corresponding to G1, G2, G3, G4 and G5 catalyst are mentioned in Table 7.1.

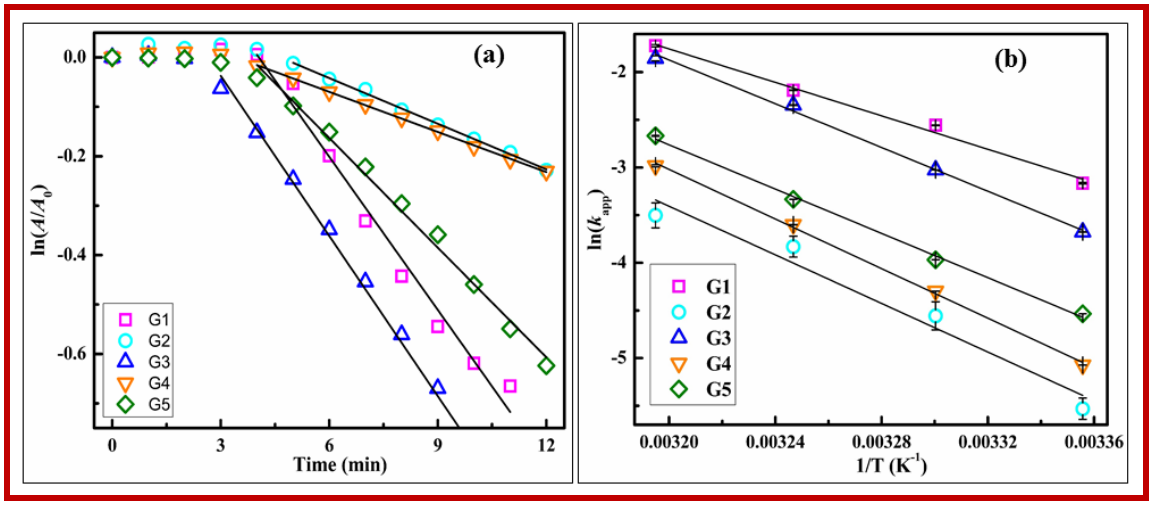

Figure 7.8 Variation of $\ln(A/A_0)$ [absorbance (A) measured at ~ 401 nm] Vs time with $NaBH_4$ reductant **8 (a)**. Arrhenius plot for Nip reduction reaction catalyzed by G1, G2, G3,

G4 and G5 samples with reducing agents $NaBH_4$ **8 (b)**. The R^2 value of all the fittings is ~ 0.98.

The Nip reduction kinetics was investigated at four different temperatures to calculate the activation energies associated with different catalyst as per linearized Arrhenius equation [Eqn. 3.4, Chapter-3]. The activation energies calculated are tabulated in Table 7.1. Except G1, rest of the activation energy values is not very different from each other. The k_{app} values obtained for G1 and G3 (1 : 1 Ag : Cu) are higher than those obtained from others. However, the TOF value obtained for G3 is the highest. Furthermore, it is higher than those found for either G1 or G5. Therefore, G3 shows synergistic catalytic activity for Nip reduction by $NaBH_4$. It is important to point out that the E_a value obtained with catalyst G1 is lower than that obtained when the reaction was catalyzed by G3. This indicates that the higher TOF value for the reaction catalyzed by G3 must be due to higher density of catalytically active sites in this BNPs/rGO composite. This could also be because of higher density of phase boundaries (as observed in Chapter-6), which give rise to more number catalytically sites.

Table 7.1. Average particle sizes, apparent reaction rate constant, activation energy and turnover frequency (TOF) for thermal Nip reduction with $NaBH_4$ at 306 K in presence of G1, G2, G3, G4 and G5 catalyst.

Catalyst	Particle size (d) (nm)	Activation energy (E_a) (kJ/mol)	Apparent reaction rate constant (k_{app}) (min^{-1})	TOF (min^{-1})
G1	~ 25	~ 73.2	0.103	~ 184.0
G2	~ 30	~ 106.1	0.031	~ 96.0
G3	~ 40	~ 95.3	0.108	~ 225.0
G4	~ 35	~ 108.1	0.027	~ 74.0
G5	~ 45	~ 97.2	0.074	~ 98.0

7.3.3.2 Methyl orange oxidation thermal and photocatalytic

Figure 7.9 shows the UV-visible spectrum of MO degradation when the reaction is carried out in presence of G3 catalyst. The peaks present initially in the UV-visible spectrum of MO in acidic medium undergo degradation with progress of time. Moreover, there is no emergence of any new absorption in this region. This suggests that MO degradation definitely occurs till stage (E, F, G) indicated in Chapter-3 (Fig. 3.16).

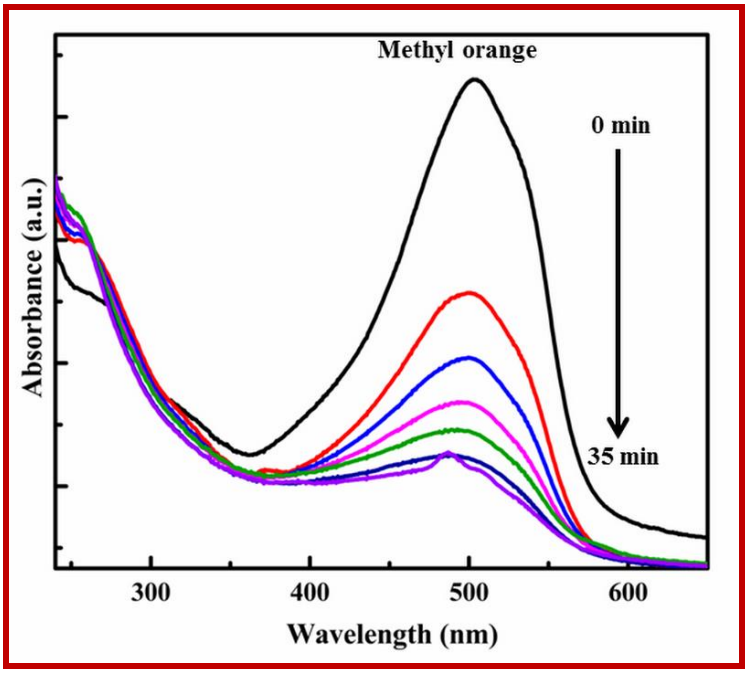

Figure 7.9 Variation of absorbance maximum of MO (~ 506 nm) with H_2O_2 oxidizing agent in presence of catalyst G3 catalyst.

The order of MO degradation by the procedure outlined in Eqn. 3.3, Chapter-3 is found to be 0 for both thermally catalyzed and photocatalyzed MO degradation. Accordingly, the k_{app} values are found from the slopes of the linear fits of A/A_0 versus time, for thermal and photocatalytic MO degradations (Figure 7. 10).

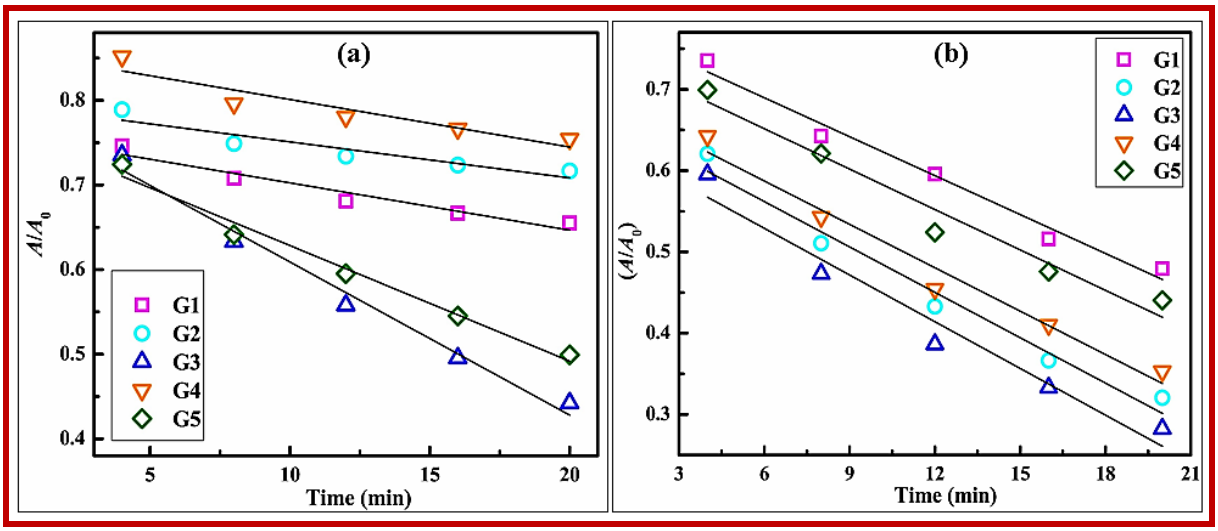

Figure 7.10 Variation of A/A_0 [absorbance (A) measured at 506 nm] versus time for thermal (a) and photocatalytic (b) MO degradation in presence of G1, G2, G3, G4 and G5 catalyst. The R^2 value of all the fittings is ~0.97.

The apparent reaction rate constants obtained from the linear fits of plots mentioned in Figure 7.10 are tabulated in Table 7.2. The MO degradation was carried out in absence of light at different temperatures to find the activation energies by utilizing the linearized Arrhenius equation given in Chapter-3 [Eqn.3.4]. The slope of the linear fits to the between $\ln(k_{app})$ and 1/T (Figure 7.11) is used to calculate the activation energy values. The activation energy in presence of G1, G2, G3, G4 and G5 catalysts are mentioned in Table 7.2. In terms of k_{app} values, both catalyzed and photocatalyzed MO oxidation reaction in presence of catalyst G3 exhibits greater activity than others.

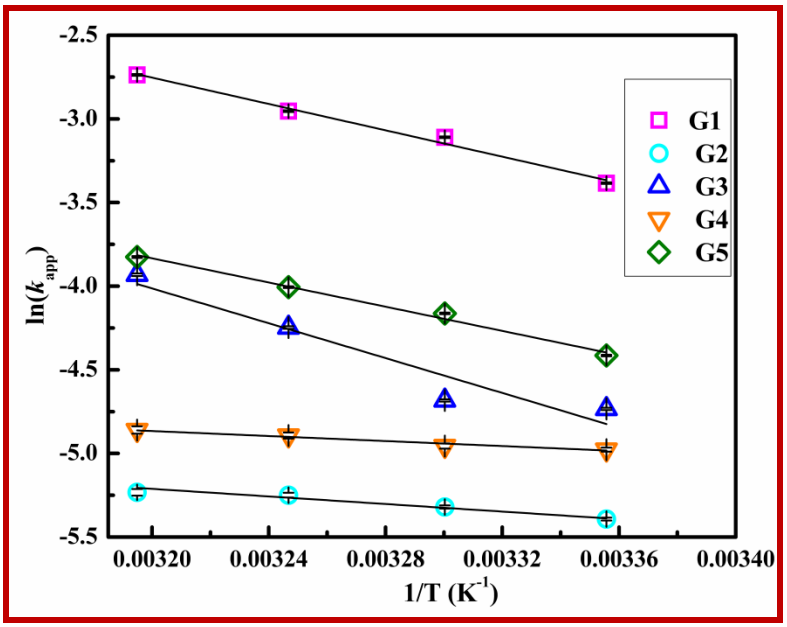

Figure 7.11 Arrhenius plot for MO degradation catalyzed by G1, G2, G3, G4 and G5 samples. Error bars are very small in most cases. The R^2 value of all the fittings is ~ 0.98.

Table 7.2 Apparent reaction rate constant, activation energy and turnover frequency (TOF) for thermal and photocatalytic MO degradation at 306 K in presence of G1, G2, G3, G4 and G5 catalyst

Catalyst	Apparent reaction rate constant (k_{app}) (mol lit^{-1} min^{-1})		Activation energy (E_a) (kJ/mol)	TOF (min^{-1})	
G1	0.0056	0.0159	33	12	15
G2	0.0043	0.0186	9	7	14
G3	0.018	0.0192	44	15	18
G4	0.0056	0.0178	6	5	12
G5	0.014	0.0166	30	10	8

For the thermal Fenton like MO degradation, G3 acts as the best catalyst. It is important to note that the catalytic activities demonstrated by G1 and G5 are also good. However, the activities decrease for other BNPs (G2 and G4). On the other hand, when the reactions were carried out under visible light the results obtained were quite different. The

visible light photocatalytic enhancement was quite dramatic. The PTOF for MO degradation is double of the TOF value obtained when G2 was used as the catalyst. While the change was still greater when G4 was used as the catalyst. That is, the PTOF value in this case is about 140 % of the TOF value. Obviously, the presence of rGO in the composite is responsible for this significant increase. Since the precursor composition of G4 is Ag : Cu ratio 1 : 2, therefore, this photocatalyst is quite economical and efficient. It appears that plasmonically excited electrons are quite efficiently transported by rGO to the hydrogen peroxide adsorbed on it for the reaction to possibly take place by the mechanism described in Chapter-3. Thus, the efficient charge separation due to rGO is responsible for the increase in photocatalytic enhancement. However, when G5 was used as the photocatalyst then there was no enhancement in activity, rather a small decrease can be observed. This means that the bimetallics of Ag-Cu are contribute to the photocatalytic activity in some synergistic way only when Ag is present.

7.4 Conclusions

The mono and bimetallic Ag/Cu, M/rGO composites were prepared by consecutive steps of adsorption of the precursor metal salts on to GO followed by chemical reduction by strong reducing agent. BNPs with fine sizes were obtained. The size of BNPs generally increased with Cu content in it. The best catalytic activity for Nip reduction by $NaBH_4$ was obtained when G3 was used the catalyst. However, Nip did not undergo reduction in presence of any of the BNPs/rGO catalysts. To understand this phenomena better, it is essential to compare the results with those obtained for BNPs in Chapter-3. The comparison indicates, that possibly Nip reduction by Gly did not occur because of lack of adsorption of Gly on rGO. For MO degradation the results are quite interesting. Here also G3 displays the

best catalytic activity. However, as seen for Nip reduction by $NaBH_4$, G1 also demonstrates good catalytic activity. In contrast to this, G5 also shows catalytic activity for MO degradation. The photocatalytic enhancement is quite strong when the reaction is carried out in presence of G2 and G4. But G3 remains the best photocatalyst for Fenton like MO degradation. No photo-enhancement in catalytic activity could observe for G5, that is Cu/rGO. The presence Ag in the BNPs coupled to rGO is, therefore, essential for synergistic enhancement in photocatalytic activity and transport of plasmonically excited electrons to hydrogen peroxide molecules adsorbed on to rGO. It seems that rGO facilitates more efficient charge separation of these plasmonically excited electrons.